Cell Reports
Physical Science

CellPress
OPEN ACCESS

Article

Fabrication of long-life quasi-solid-state Na-CO_2 battery by formation of $Na_2C_2O_4$ discharge product

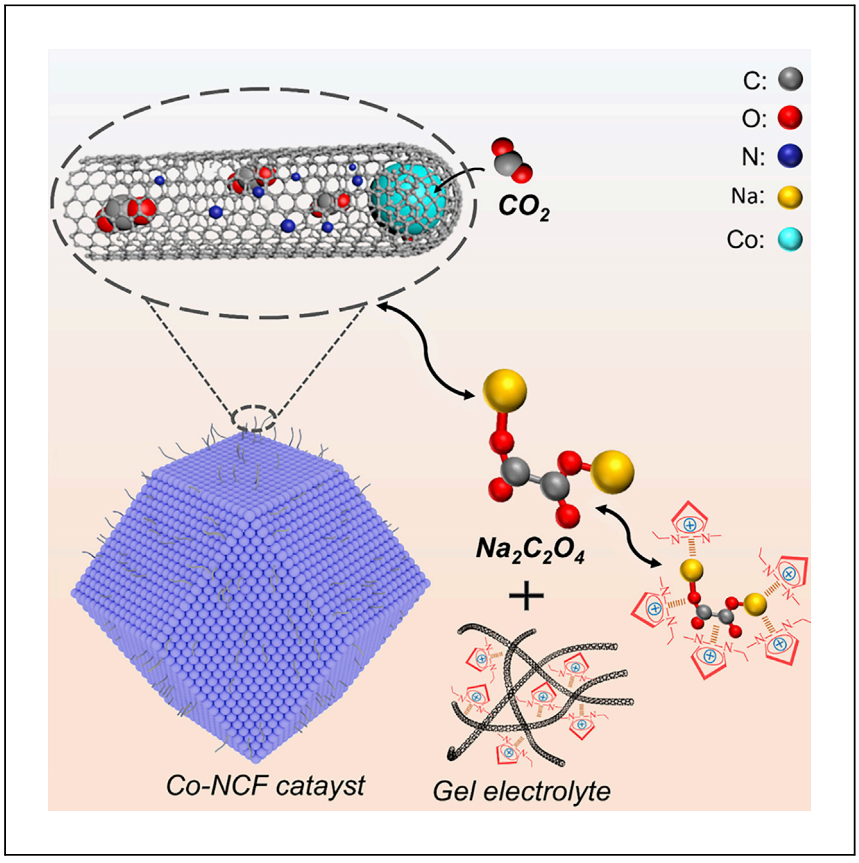

Liang et al. report a simple strategy to facilitate the formation of $Na_2C_2O_4$ discharge products in Na-CO_2 batteries. Through the synergistic effect of a Co-encapsulated N-doped carbon framework catalyst and gel electrolyte, the quasi-solid-state Na-CO_2 battery exhibits high discharge capacity, high rate, and excellent cycling performance.

Bowen Xu, Da Zhang, Shilei Chang, ..., Bin Yang, Yong Lei, Feng Liang

liangfeng@kust.edu.cn

Highlights

$Na_2C_2O_4$ is discharge product by design of catalyst and electrolyte in Na-CO_2 battery

Co in Co-NCF catalyst changes the conventional CO_2RR pathway to form $Na_2C_2O_4$

Gel stabilizes $Na_2C_2O_4$ by charge transfer from $Na_2C_2O_4$ to organic cations

Na-CO_2 battery has large discharge capacity, high rate, and good cycling performance

Xu et al., Cell Reports Physical Science 3, 100973
July 20, 2022
https://doi.org/10.1016/j.xcrp.2022.100973

Cell Reports
Physical Science

CellPress
OPEN ACCESS

Article

Fabrication of long-life quasi-solid-state Na-CO_2 battery by formation of $Na_2C_2O_4$ discharge product

Bowen Xu,[1,2,5] Da Zhang,[1,2,5] Shilei Chang,[1,2] Minjie Hou,[1,2] Chao Peng,[3] Dongfeng Xue,[3] Bin Yang,[1,2] Yong Lei,[4] and Feng Liang[1,2,6,*]

SUMMARY

Rechargeable Na-CO_2 batteries are promising energy-storage devices due to their high energy density, environmental friendliness, and cost effectiveness. However, the insulating nature and irreversibility of the Na_2CO_3 discharge product cause large polarization and poor cyclicity. Here, we report a reversible quasi-solid-state Na-CO_2 battery that is constructed by the synergistic action of a Co-encapsulated N-doped carbon framework catalyst and gel electrolyte to ensure the formation of a highly reversible $Na_2C_2O_4$ discharge product. Experiments and density functional theory calculations indicate that the electron-agglomeration effect of Co nanoparticles enhances CO_2 adsorption and lowers energy barrier, as well as promotes $Na_2C_2O_4$ generation. A gel electrolyte containing an imidazole organic cation is used to inhibit the decomposition of the thermodynamically unstable $Na_2C_2O_4$. The fabricated Na-CO_2 battery exhibits a high discharge capacity of 3,094 mAh g^{-1}, a high-rate performance of 1,777 mAh g^{-1} at a current density of 0.5 mA cm^{-2}, and excellent cycling performance of 366 cycles (2,200 h).

INTRODUCTION

Metal-CO_2 batteries have attracted immense attention due to their capability to convert contaminated gas such as CO_2 into energy resources via a "clean" strategy.[1–3] Additionally, due to the abundance of sodium resources, the Na-CO_2 battery has great potential as a portable energy-storage device because of its low charging voltage compared with that of a Li-CO_2 battery.[4,5] However, Na_2CO_3, being considered as the final discharge product in a Na-CO_2 battery, is insulating and thermodynamically stable. Its slow and incomplete decomposition severely blocks gas-diffusion channels during the charging process, forming an irreversible Na-CO_2 battery with a large overpotential and poor cycling performance.[6,7] Thus, it is vital to overcome the insulating drawback of Na_2CO_3 and hence to accelerate the practical application of Na-CO_2 batteries.

Until recently, subtly changing the discharge products has been considered a more effective strategy to overcome the limitations of the discharge product of Na_2CO_3 than enhancing the reduction performance of the catalyst toward it.[8,9] The more conductive and easily decomposed oxalate ($C_2O_4^{2-}$) has been identified as a good substitute for carbonate (CO_3^{2-}); the capacity retention and cycling performance of Na-CO_2 batteries could be significantly improved by generating $C_2O_4^{2-}$ as the final discharge product. Hence, the simultaneous generation and stabilization of $C_2O_4^{2-}$ for improving the performance of Na-CO_2 batteries is challenging. Previous

[1]The National Engineering Research Center for Vacuum Metallurgy, Kunming University of Science and Technology, Kunming 650093, China

[2]Faculty of Metallurgical and Energy Engineering, Kunming University of Science and Technology, Kunming 650093, China

[3]Multiscale Crystal Materials Research Center, Shenzhen Institute of Advanced Technology, Chinese Academy of Sciences, Shenzhen 518055, China

[4]Institute of Physics and IMN MacroNano, Ilmenau University of Technology, Ilmenau 98693, Germany

[5]These authors contributed equally

[6]Lead contact

*Correspondence: liangfeng@kust.edu.cn

https://doi.org/10.1016/j.xcrp.2022.100973

research reported an effective strategy of mitigating the disproportionation of $C_2O_4^{2-}$ by the charge-transfer interaction of a special catalyst with oxalate.[10,11] However, this strategy severely limits the selection of catalysts, which is unsuitable for a lot of catalysts with stronger catalytic properties but without the ability to stabilize $Na_2C_2O_4$. Consequently, there is an urgent need for a general approach to construct metal-CO_2 batteries with $C_2O_4^{2-}$ as the final discharge product, promoting their large-scale applications.

In this study, a highly reversible quasi-solid-state Na-CO_2 battery with $Na_2C_2O_4$ as the final discharge product is constructed through a rational design of cathode system. Co nanoparticles in catalysts of Co-encapsulated N-doped carbon framework (Co-NCF) promote the formation of a highly reversible $Na_2C_2O_4$ discharge product, as indicated by experimental techniques (spectroscopy and electrochemical analysis) and density functional theory (DFT) calculations. Subsequently, the $Na_2C_2O_4$ generated *in situ* is stabilized via interactions with organic cations in the gel electrolyte, retarding the transformation of $Na_2C_2O_4$ to Na_2CO_3. The fabricated quasi-solid-state Na-CO_2 battery exhibits a large discharge capacity of 3,094 mAh g^{-1}, a high-rate performance (1,777 mAh g^{-1} at a current density of 0.5 mA cm^{-2}), and excellent cycling performance of 367 cycles (2,200 h) at a current density of 0.1 mA cm^{-2}. This study provides a feasible and efficient route of promoting $Na_2C_2O_4$ as the final discharge product through rational designing the cathode system, which shall be helpful for future research further developing metal-CO_2 batteries.

RESULTS

Physical and chemical properties of Co-NCF catalyst

The X-ray diffraction (XRD) analysis, which was performed to determine the composition of Co-NCF (Figure 1A), indicated the presence of Co, with distinct peaks at 44.1°, 51.7°, and 75.8° corresponding to the (111), (200), and (220) planes of metallic Co nanoparticles, respectively (JCPDS no. 15-0806).[12] A peak was observed at 26.2°, corresponding to the graphite (002) plane. Scanning electron microscopy (SEM) images with different magnifications indicated that the Co-NCF exhibited polyhedral morphology, with a rough surface containing carbon nanotube (CNT) growth (Figures 1B and 1C). The fine network of crystalline CNTs improved the efficiency of the mass transfer and electronic conductivity.[13–15] Transmission electron microscopy (TEM) was used to further elucidate the morphology and size of Co-NCF, whereby it exhibited a highly uniform dodecahedral morphology with an average size of about 570 nm (Figures 1D and 1E). Its high-resolution TEM (HRTEM) image (Figure 1F) indicated interplanar distances of 0.182 and 0.37 nm corresponding to the (200) planes of metallic cobalt and (002) planes of graphitic carbon, respectively. Selected-area electron diffraction (SAED) showed that the as-prepared Co-NCF was polycrystalline. Additionally, high-angle annular dark-field scanning TEM (HAADF-STEM) images (Figures 1G–1J) indicated the homogeneous dispersion of Co, C, and N in Co-NCF. The chemical compositions of the N dopants were investigated using X-ray photoelectron spectroscopy (XPS); the results indicated that the synthesized Co-NCF consisted of Co, C, and N (Figure S1). As shown in Figure 1K, the N 1s spectrum was decomposed into three types of nitrogen peaks corresponding to 398.76, 399.96, and 401.40 eV for pyridinic N, pyrrolic N, and graphitic N, respectively.[16,17] A large interaction between pyridine N and CO_2 molecules could improve the CO_2 absorption, pyrrolic N could effectively adsorb Na^+, and graphitic N could improve the Co-NCF conductivity.[18–20] The Co $2p_{3/2}$ spectrum showed three fitting peaks at 782.94, 780.63, and 778.52 eV

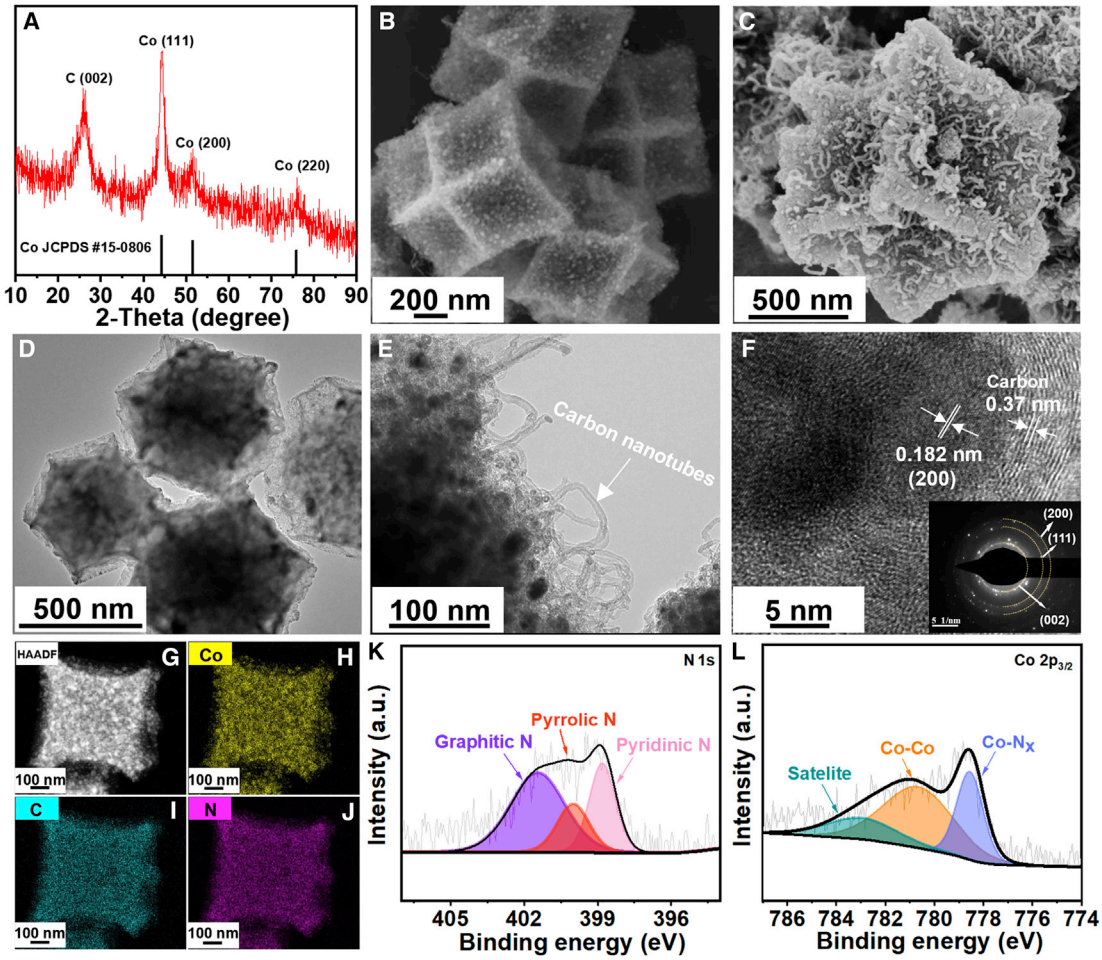

Figure 1. Characterization of Co-NCF catalyst

(A) XRD patterns of Co-NCF.

(B and C) SEM images of Co-NCF at different magnifications.

(D and E) TEM images of Co-NCF at different magnifications.

(F) HRTEM image of Co-NCF. Inset: SAED pattern of Co-NCF.

(G–J) HAADF-STEM image of Co-NCF (G) and corresponding element mappings of (H) Co, (I) C, and (J) N.

(K and L) XPS spectra of (K) N 1s and (L) Co $2p_{3/2}$ in Co-NCF.

corresponding to the satellite Co state, Co-N_x, and Co-Co, respectively, which determined the reaction route, as discussed later (Figure 1L).[21,22] Based on N_2 adsorption-desorption isotherms, the specific surface area (SSAs) of the Co-NCF was 1,263 m^2 g^{-1}. Furthermore, Barrett-Joyner-Halenda (BJH) analysis indicated an average pore diameter of 30 nm (Figure S2), thus enabling good adsorption by the Co-NCF catalysts and providing sufficient active sites for the electrochemical conversion of CO_2.[23–25]

Physical and chemical properties of gel electrolyte

The gel electrolyte is a material consisting of two or more components (one of which is a liquid) and is soft, solid, or solid-like in nature.[26] Herein, a gel electrolyte with highly ionic conductivity was designed to obtain better electrochemical performance of the quasi-solid-state Na-CO_2 battery. A TEM image of the original CNT (Figure S3) indicated that they were entangled with each other, forming complex bundles due to strong van der Waals forces.[27] Upon gelation, the entangled CNT

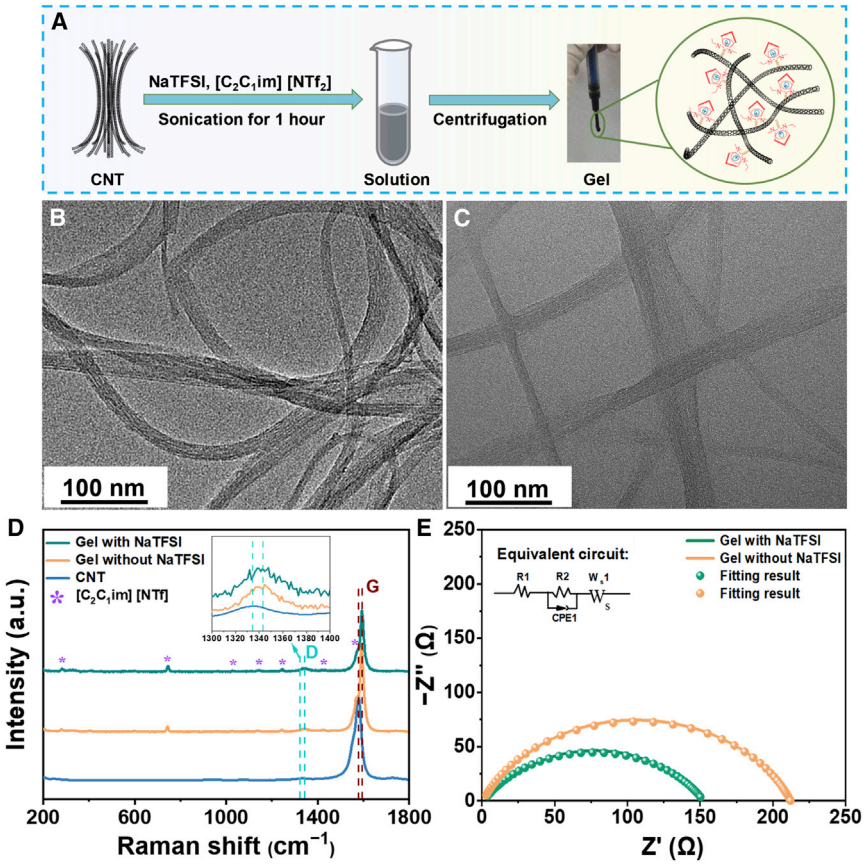

Figure 2. Characterization of gel electrolyte

(A) Preparation of gel electrolytes with NaTFSI.

(B) TEM image of a gel without NaTFSI.

(C) TEM image of a gel with NaTFSI.

(D) Raman spectral curves of the gels (with and without NaTFSI).

(E) EIS curves of the gels (with and without NaTFSI).

bundles formed a three-dimensional (3D) network due to the interaction of the organic cations in the imidazolium ion group of the 1-ethyl-3-methyl imidazolium ($[C_2C_1im]$) bis (trifluoromethylsulfonyl) imide ($[NTf_2]$) ionic liquid (IL) with the π electrons of CNT (Figure 2A).[28] In addition, given its high electrical conductivity (10^2–10^3 S cm^{-1}), CNTs serve as electron conduction channels for gel electrolytes.[29,30]

Physical properties of the as-prepared gel electrolyte were characterized, as shown in Figures 2B and 2C. In this study, unlike previous work, NaTFSI was added to the gel electrolyte to increase ionic conductivity.[31] No significant changes in morphology were observed after the addition of NaTFSI, indicating a negligible influence of NaTFSI on the formation of the gel electrolyte. Figure 2D shows the Raman spectra of the original CNT and the gel (with and without NaTFSI); two typical peaks of the D and G bands were detected, corresponding to the tangential vibrations of the carbon atoms in the nanotubes and the defects of the carbon atom lattice, respectively.[32] The D and G bands of the gels were shifted to a slightly higher region compared with those of the pure CNTs, attributed to the transfer of the CNT surface electrons to the electron-deficient imidazolium ions in the $[C_2C_1im][NTf_2]$ IL during gel formation.[33] Electrochemical impedance spectroscopy (EIS) was used to investigate the ionic transfer dynamics, as shown in Figure 2E. The gel with NaTFSI

exhibited a higher ionic conductivity (5.3×10^{-3} S cm^{-1}) than the gel without NaTFSI (3.8×10^{-3} S cm^{-1}), indicating enhanced migration of ionic due to NaTFSI addition. This may be due to the addition of NaTFSI leading to an extensive aggregation with the permeation path of Na cations in the gel electrolyte. The extensive aggregation allows for more rapid site exchange through a structural rearrangement, thus resulting in a higher diffusion coefficient of Na ions.[34] Figure S4 shows the linear sweep voltammetry (LSV) curves of the gels with and without NaTFSI. The electrochemical window of the gel with NaTFSI (4.2 V) was slightly lower than that of the gel without NaTFSI (4.5 V), possibly due to the decomposition of NaTFSI. However, these values of the gel with NaTFSI indicated better electrochemical performance and sufficient thermal stability for the practical application of a quasi-solid-state Na-CO_2 battery (Figures S5–S7). It is worth noting that the addition of NaTFSI would not affect the species of discharge products (Figure S8). Therefore, the gel with NaTFSI is used in the quasi-solid-state Na-CO_2 battery.

Electrochemical performance of quasi-solid-state Na-CO_2 batteries

To understand the catalytic effect of N-CNT, the rhombic dodecahedron structure of NCF and Co nanoparticles on the CO_2 reduction reaction (CO_2RR) pathway in Co-NCF, quasi-solid-state Na-CO_2 batteries were prepared using a gel electrolyte with Co-NCF, NCF (Zif-8 derivative), commercial N-CNT, and commercial Ru/C catalysts (Figures S9–S15). The discharge-charge profiles of the batteries with different catalysts are shown in Figure 3A. The voltage gap of the quasi-solid-state Na-CO_2 battery using Co-NCF was ~1.7 V at the cut off voltage of 4 V, lower than that of NCF, N-CNT, and Ru/C catalysts. This indicates that the Co nanoparticles in the Co-NCF catalyst can significantly improve the overall performance of the battery. The discharge capacities of the batteries were tested at a current density of 0.1 mA cm^{-2} with a cut off voltage of 1 V (Figure 3B). The battery with the Co-NCF catalyst exhibited a higher discharge capacity of 3,094 mAh g^{-1} at 0.1 mA cm^{-2}, approximately 2.33, 2.94, and 4.19 times higher than that of N-CNT (1,330 mAh g^{-1}), Ru/C (1,051 mAh g^{-1}), and NCF (738 mAh g^{-1}), respectively. The high discharge capacity of the quasi-solid-state Na-CO_2 battery with the Co-NCF catalyst could be attributed to the high SSAs of Co-NCF, accommodating more discharge products and alleviating gas blockages. Additionally, the catalyst is covered by the discharge products during the discharge process, resulting in active-site inactivation. Unlike the insulated Na_2CO_3, $Na_2C_2O_4$ with high electron conductivity can alleviate catalyst active-site inactivation.[35,36]

Figures 3C and S16 show the rate performance of the quasi-solid-state Na-CO_2 batteries with different catalysts. Surprisingly, the quasi-solid-state Na-CO_2 battery with the Co-NCF catalyst exhibited a large discharge capacity (1,777 mAh g^{-1}) at a high current density (0.5 mA cm^{-2}), attributed to weak catalyst poisoning and the presence of abundant catalytic active sites (Co nanoparticles). As shown in Figures 3D and S17, the cycle lives of quasi-solid-state Na-CO_2 batteries with different catalysts were tested. The battery with the Co-NCF catalyst exhibited better cyclicity (more than 367 cycles at 0.1 mA cm^{-2}) than the quasi-solid-state Na-CO_2 batteries with the NCF (26 cycles), N-CNT (32 cycles), and Ru/C (74 cycles) catalysts. This improved cyclicity could be attributed to good reversibility of the discharge product. Additionally, the discharge capacity-retention rates of the quasi-solid-state Na-CO_2 batteries with different catalysts were examined at a current density of 0.1 mA cm^{-2} with cut off voltages in the range of 1 to 4 V (Figure 3E). The discharge capacity retention of the Co-NCF catalyst was 78.2%, which was higher than that of N-CNT (24.5%), Ru/C (42%), and NCF (38.4%). EIS was used to investigate the impedance change of the quasi-solid-state Na-CO_2 batteries with the Co-NCF, N-CNT, and NCF catalysts

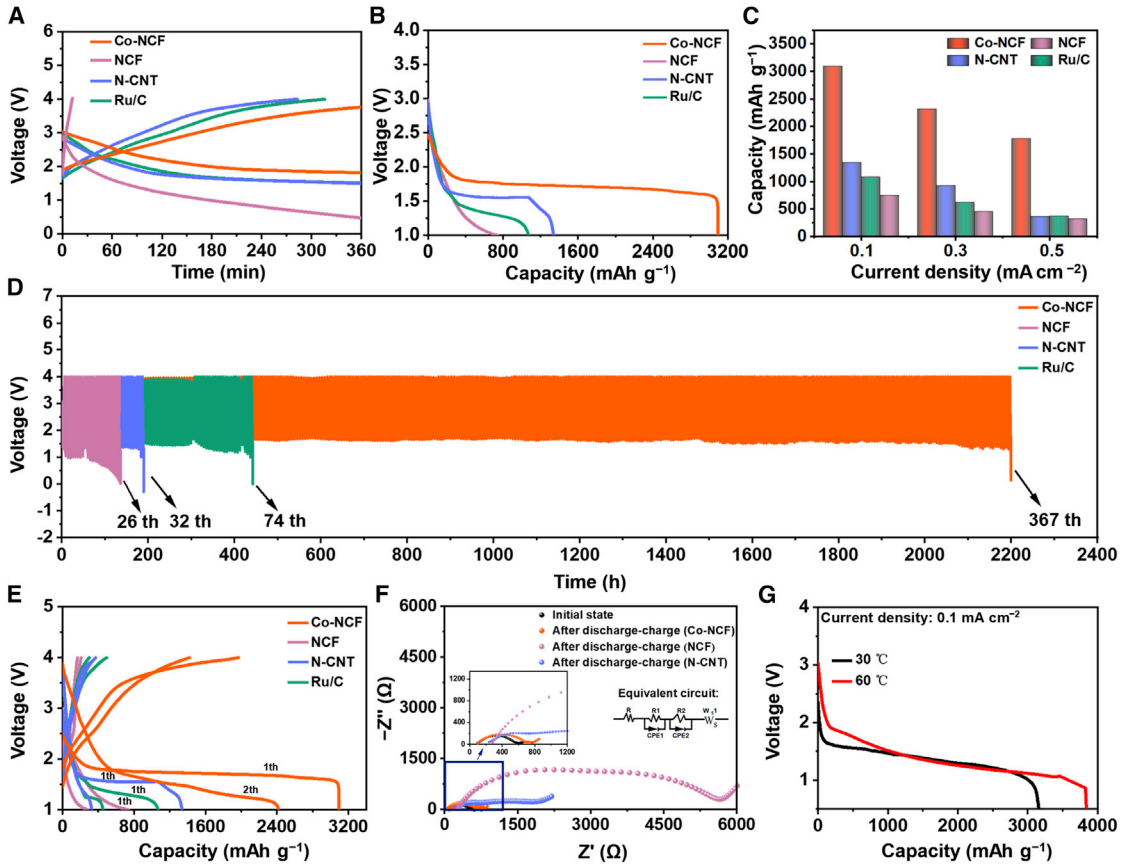

Figure 3. The electrochemical performance of the quasi-solid-state Na-CO_2 batteries

(A) Voltage gap curves of batteries with different catalysts at a current density of 0.1 mA cm^{-2}.

(B) Discharge capacity of batteries with different catalysts at a current density of 0.1 mA cm^{-2}.

(C) Rate performance of batteries with different catalysts.

(D) Cycling performance of batteries with different catalysts at a current density of 0.1 mA cm^{-2}, with a discharge-change time of 3 h.

(E) Capacity retention rate with different catalysts at a current density of 0.1 mA cm^{-2}.

(F) Alternating current (AC) impedance spectrum curves of batteries with different catalysts.

(G) Discharge capacity curves with Co-NCF at different temperatures.

after discharge charge (Figure 3F). A slight increase in the total resistance (77 Ω) of the Na-CO_2 battery with the Co-NCF catalyst after discharge charge was observed, indicating easier decomposition of the discharge product.[37,38] On the other hand, the Co-NCF catalyst exhibited a high discharge capacity of 3,837 mAh g^{-1} at 60°C, indicating good high-temperature stability of the quasi-solid-state battery with Co-NCF (Figure 3G).

Product characterization of battery reactions

To determine the influence of the cathode system on the charge and discharge process and reaction mechanism of the Na-CO_2 battery, the discharge products were studied in depth by *in situ* Raman and *ex situ* XPS. As shown in Figure 4A, there is a weak peak at 1,090 cm^{-1} in the initial state and no significant change during the charging/discharging process, which is regarded as the peak of binder (polytetrafluoroethylene [PTFE]) in the gas-diffusion layer (Figure S18). Interestingly, a new characteristic peak corresponding to C–C bond of $C_2O_4^{2-}$ was detected at 893 cm^{-1} with increasing discharge time, suggesting the production of $Na_2C_2O_4$.[39] The peak intensity of $Na_2C_2O_4$ gradually increases with increasing

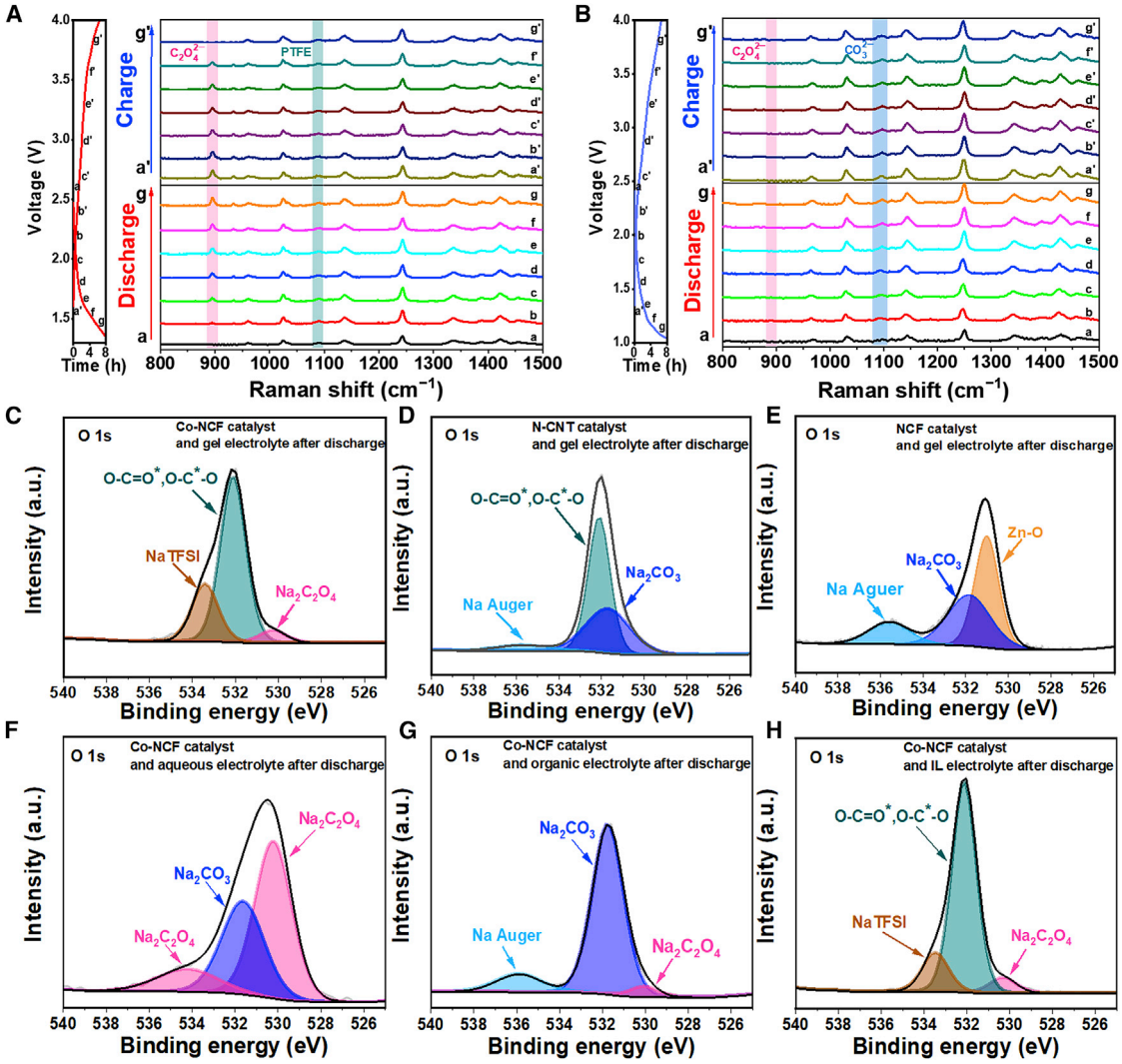

Figure 4. Characterization of discharge products of quasi-solid-state Na-CO_2 batteries

(A) *In situ* Raman spectra of quasi-solid-state Na-CO_2 batteries with Co-NCF catalyst and gel electrolyte.

(B) *In situ* Raman spectra of quasi-solid-state Na-CO_2 batteries with N-CNT catalyst and gel electrolyte.

(C–E) *Ex situ* O 1s XPS spectra of quasi-solid-state Na-CO_2 batteries using different catalysts and the gel electrolyte.

(F–H) *Ex situ* O 1s XPS spectra of Na-CO_2 batteries using the Co-NCF catalyst and different electrolytes.

discharge time compared with the peak of $Na_2C_2O_4$ that disappears during the subsequent charging process, indicating the presence of $Na_2C_2O_4$ and the complete removal of $Na_2C_2O_4$ during the first discharge and charge.

In addition, $Na_2C_2O_4$ was still the discharge product in the quasi-solid Na-CO_2 battery after long cycling by *ex situ* XRD analysis (Figure S19). Thus, $Na_2C_2O_4$ was the final discharge product in the quasi-solid-state Na-CO_2 battery with the Co-NCF catalyst and gel electrolyte. The following reactions occurred in the battery (Equation 1):

$$2Na^+ + 2CO_2 + 2e^- \leftrightarrow Na_2C_2O_4 \quad \text{(Equation 1)}$$

As can be seen from Figure 4B, the intensity of the characteristic peak (C–O bond of carbonate) at 1,090 cm^{-1} gradually increased during the discharge process when the

N-CNT was used as catalyst.[40] However, the intensity of the peak did not decrease to the initial state during the charging process, which indicates the formation and incomplete decomposition of Na_2CO_3. This is the same result as that obtained with the NCF catalyst (Figure S20). This indicated that the quasi-solid-state Na-CO_2 batteries with NCF or N-CNT catalyst proceeded according to the chemical reaction of Equation 2.

$$4Na^{+} + 3CO_2 + 4e^{-} \rightarrow 2Na_2CO_3 + C \quad \text{(Equation 2)}$$

To further explore the effect of Co-NCF catalysts on the discharge products, the discharge products of quasi-solid-state Na-CO_2 batteries are characterized by *ex situ* XPS (Figures 4C–4H). As shown in Figure 4C, it was found that one fitting peak located at 530.4 eV corresponding to $C_2O_4^{2-}$ was observed for quasi-solid-state Na-CO_2 battery with Co-NCF catalyst and gel electrolyte, which was consistent with O 1s spectrum of commercial $Na_2C_2O_4$ (Figure S21), indicating the generation of $Na_2C_2O_4$. Although $Na_2C_2O_4$ cannot be detected for the discharge products with the N-CNT or NCF catalyst, a significant peak of 531.7 eV (Na_2CO_3) was observed (Figures 4D and 4E).[41] This also verifies that Co nanoparticles of Co-NCF catalyst significantly determine the discharge products of quasi-solid-state Na-CO_2 batteries.

To investigate the effect of electrolyte on generation of $Na_2C_2O_4$, the discharge products of Na-CO_2 batteries with Co-NCF catalyst and aqueous electrolyte (saturated NaCl), organic electrolyte (tetraethylene glycol dimethyl ether) were subsequently analyzed (Figures 4F and 4G). Two fitting peaks of $Na_2C_2O_4$ and Na_2CO_3 can be obtained from O 1s XPS spectrum, which is consistent with the Raman results (Figures S22A and S22B), suggesting that a disproportionation reaction occurred (Equation 3). Therefore, it is reasonable to believe that there is a charge transfer between the imidazole-based organic cations in the gel and the *in situ* generated $Na_2C_2O_4$, which reduced the charge density of $Na_2C_2O_4$ and relieved $Na_2C_2O_4$ from the disproportionation reactions. This also can be verified from the discharge products ($Na_2C_2O_4$) with [C_2C_1im][NTf_2] IL electrolyte (Figures 4H and S22C). It is notable that although [C_2C_1im][NTf_2] IL can be used as an electrolyte to stabilize $Na_2C_2O_4$, its liquid character leads to electrolyte-leakage safety issues.[42] In addition, its poor conductivity increases the energy barrier of CO_2RR, which is not a good candidate for the real application of Na-CO_2 batteries (Figure S23).[43,44]

$$2Na_2C_2O_4 \rightarrow 2Na_2CO_3 + C + CO_2\uparrow \quad \text{(Equation 3)}$$

DFT calculations

DFT calculations were used to identify the origin of the high catalytic performance of Co-NCF and provide an in-depth understanding of its selective CO_2RR activity. According to XRD and SAED, the (111), (200), and (220) planes were the primary exposed crystal planes of the Co nanoparticles on the NCF catalyst, while the primary crystal plane of NCF was characterized as the graphitic carbon (002) plane. Additionally, XPS analysis indicated that the major speciation of nitrogen in the graphitic carbon (002) layer involved graphitic N, pyridinic N, and pyrrolic N. Figure S24 shows the top view of different Co nanoparticle surfaces of the Co-NCF structure. The Co nanoparticles were exposed on the carbon surface, consistent with the experimental results, confirming the structure. Notably, *in situ* Raman results and the adsorption-desorption isotherm of CO_2 indicated that the Co nanoparticles in Co-NCF played a significant role in the selective CO_2RR activity and CO_2 chemisorption (Figure S25). Subsequently, the adsorption energies of CO_2 at the different surfaces of the Co nanoparticles in Co-NCF were analyzed (Figure S26).

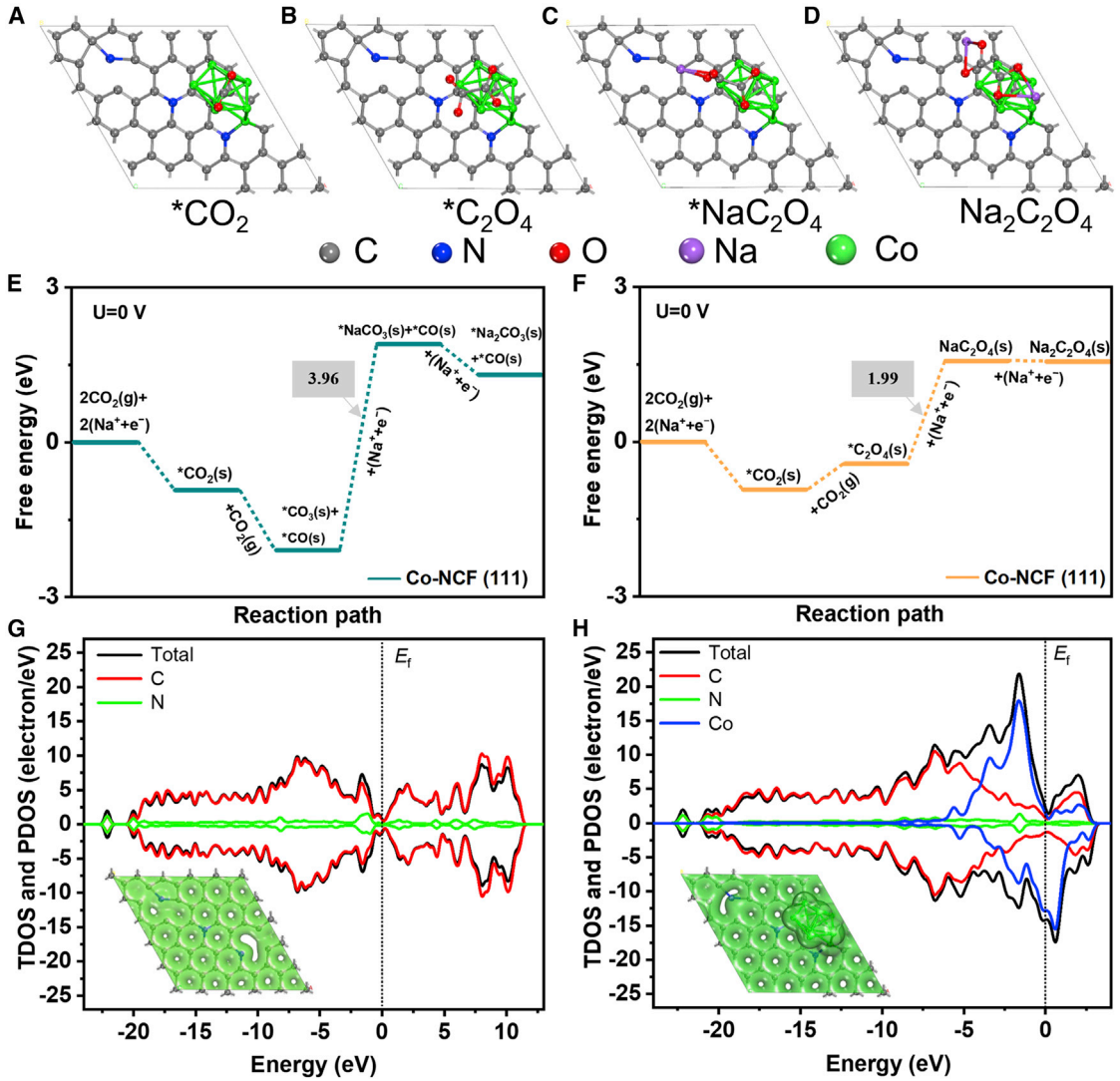

Figure 5. DFT study of Co-NCF

(A–D) *CO_2 adsorption on Co-NCF (111) (A), *C_2O_4 adsorption on Co-NCF (111) (B), *NaC_2O_4 adsorption on Co-NCF (111) (C), and *$Na_2C_2O_4$ adsorption on Co-NCF (111) (D). The asterisk represents the adsorption state.

(E and F) Calculated energetic profiles of (E) Na_2CO_3 and (F) $Na_2C_2O_4$ nucleation on the Co-NCF (111) surfaces at U = 0 V. The Fermi level is indicated by a vertical line.

(G and H) The total and partial density of states (TDOS and PDOS) of NCF and Co-NCF (111), respectively. The inserts show charge density image of (G) NCF and (H) Co-NCF (111).

The highest adsorption energy was −1.09 eV on Co (111), indicating more probable catalytic sites for CO_2RR.[45,46]

The reaction pathways of the CO_2RR processes were also elucidated by analyzing the reaction thermodynamics. The adsorption structures of the intermediates are shown in Figures 5A–5D and S27. Figures 5E and 5F show the CO_2RR Gibbs free energy (ΔG) on the (111) surface of Co-NCF with the correlative nucleation of $Na_2C_2O_4$ and Na_2CO_3, triggered by Na^+ adsorption in the presence of electrons. Oxalate generation was the kinetically controlled step for $Na_2C_2O_4$ nucleation, while carbonate production was the kinetically rate-limiting step for Na_2CO_3 formation. The energy barriers for the controlling step of $Na_2C_2O_4$ and Na_2CO_3 nucleation were 1.99

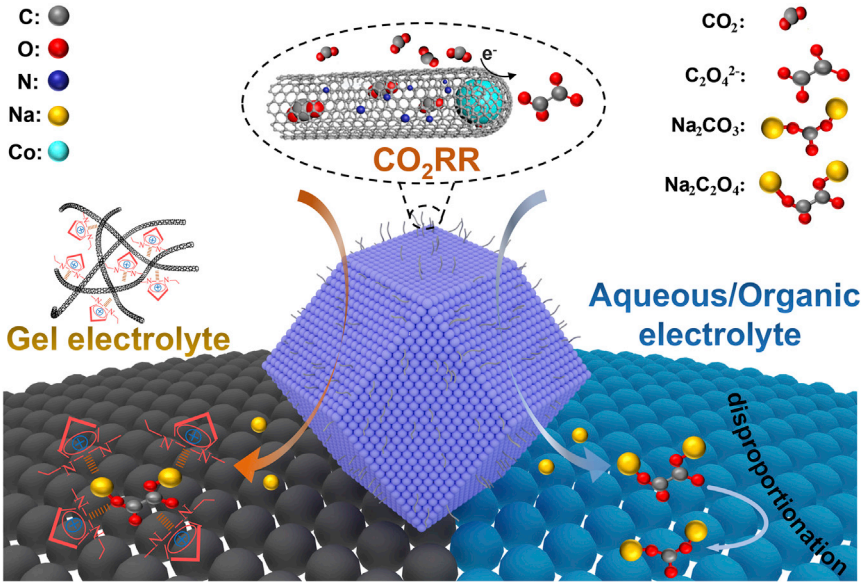

Scheme 1. Electrochemical reaction mechanism of CO_2RR in the quasi-solid-state Na-CO_2 battery

and 3.96 eV, respectively, indicating $Na_2C_2O_4$ to be the thermodynamically favored discharge product in Na-CO_2 batteries due to the presence of Co nanoparticles in the Co-NCF catalyst.[47]

The total and partial density of states (TDOS and PDOS, respectively) were calculated to understand the inherent electron variations causing the high catalytic activity of the Co nanoparticles further, as shown in Figures 5G and 5H. The TDOS and PDOS plots show the valence bands of both the up- and down-spin channels in NCF and Co-NCF near the Fermi level, indicating their metallic properties. A large amount of charge accumulated on the surface of the Co nanoparticles when they were embedded in the NCF, indicating a significant interaction between the NCF and Co nanoparticles, as was also observed in atomic force microscopy (AFM) images (Figure S28). Additionally, the PDOS indicated that the number of states across the Fermi energy level of different Co facets within NCF were significantly higher than those without Co nanoparticles (Figure S29). Thus, embedding Co nanoparticles in NCF enhanced its electrical conductivity. Charge-density differences also indicated large electron transfers between the Co nanoparticles and the NCF substrate, indicating strong chemical interactions. Charge transfer from the substrate to the adsorbate leads to effective molecule activation, thus promoting the subsequent CO_2RR.

Electrochemical reaction mechanism

The mechanism of $Na_2C_2O_4$ generation in the Na-CO_2 battery using the Co-NCF catalyst is shown in Scheme 1. During discharge, Na loses electrons to form Na^+ at the anode, reaching the cathode after passing through the sodium super ionic conductor (NASICON) ceramic separator. Due to the electronic interaction between Co and the N-doped carbon layer, a large amount of charge accumulated on the surface of the Co nanoparticles, increasing CO_2 adsorption and lowering the reaction energy barrier. Compared with the insulating Na_2CO_3, it is more favorable to generate the highly conductive $Na_2C_2O_4$ during discharge to significantly improve the capacity and rate performance of the Na-CO_2 battery. However, $Na_2C_2O_4$ is thermodynamically unstable; therefore, a gel electrolyte was used to prevent its

decomposition. In the gel electrolyte, $Na_2C_2O_4$ was surrounded by imidazole-like organic cations, significantly reducing the charge on its surface, preventing the disproportionation reaction of $C_2O_4^{2-}$ to CO_3^{2-}, and, finally, ensuring $Na_2C_2O_4$ as the final discharge product. $Na_2C_2O_4$ decomposed easily during charging, leading to a higher reversible capacity and longer cycle life of the Na-CO_2 battery. In contrast, in aqueous (saturated NaCl) or organic (tetraethylene glycol dimethyl ether) electrolytes, $Na_2C_2O_4$ was surrounded by numerous charges due to the high conductivity of the electrolytes, facilitating the disproportionation reaction to form Na_2CO_3. Consequently, it is a feasible strategy to promote $Na_2C_2O_4$ as the final discharge product by rational design of the cathode system.

DISCUSSION

In this study, using a Co-NCF catalyst and a gel electrolyte, a novel quasi-solid-state Na-CO_2 battery with $Na_2C_2O_4$ as the discharge product was constructed. Experimentation and DFT calculations indicated that electron transfer from the NCF to the adjacent Co nanoparticles promoted CO_2 adsorption and lowered the reaction energy barrier, which facilitates the production of $Na_2C_2O_4$. Subsequently, the $Na_2C_2O_4$ generated *in situ* was stabilized via interactions with organic cations in the gel electrolyte, retarding the transformation of $Na_2C_2O_4$ to Na_2CO_3. The quasi-solid-state Na-CO_2 battery constructed here exhibited a high specific capacity of 3,094 mAh g^{-1} at a current density of 0.1 mA cm^{-2}, a high-rate performance (1,777 mAh g^{-1} at a current density of 0.5 mA cm^{-2}), and excellent cycling performance of up to 367 cycles (2,200 h). This study could facilitate the future design and development of all-solid-state Na-CO_2 batteries with high stability, safety, and excellent electrochemical performance.

EXPERIMENTAL PROCEDURES

Resource availability

Lead contact

Further information and requests for resources should be directed to and will be fulfilled by the lead contact, Feng Liang (liangfeng@kust.edu.cn).

Materials availability

This study did not generate new unique reagents. All chemicals were purchased from commercial suppliers and used as received without further purification: 2-Methlimidazole (Macklin), Co $(NO_3)_2 \cdot 6H_2O$ (Aladdin), CNT (Superpure, XFNANO), Ru/C (Ru 5%, Macklin), and zinc nitrate hexahydrate (99%, Aladdin).

Data and code availability

Data supporting the findings of this paper are available from the corresponding authors upon reasonable request.

Preparation of the Co-NCF catalyst

The Co-NCF materials were synthesized according to a previous publication.[48] 2-Methlimidazole (7.88 g) was dissolved in a solvent mixture of 80 mL methanol and 80 mL ethanol to form a clear solution, while Co $(NO_3)_2 \cdot 6H_2O$ (6.984 g) was dissolved separately in the same solvent mixture to form a red solution. Subsequently, the two solutions were mixed and stirred for 60 s in a beaker and maintained at 30°C for 20 h to produce a purple precipitate. The precipitate was separated by centrifugation and dried at 80°C for 10 h. The purple ZIF-67 particles were then calcined to form Co-NCF by heating under an Ar/H_2 flow (9:1 in volume) at 350°C for 135 min, followed by maintaining the temperature at 700°C for 315 min. In order to remove the large metal clusters and excess free metals produced by the reduction of metal

cations during the pyrolysis process, the black powder produced was added to 0.5 M H_2SO_4 solution for 6 h and centrifuged to obtain the product, washed five times with distilled water, and dried at 80°C.[49,50] For comparison, an NCF was synthesized without Co by calcining ZIF-8 under the same conditions, and the detailed procedures for the NCF catalyst synthesis are provided in the supplemental experimental procedures.

Preparation of gel electrolyte

The gel electrolyte was prepared as follows. First, CNT (10 mg) and NaTFSI (330 mg) were dispersed in an $[C_2C_1im][NTf_2]$ IL (1.5 mL) by ultrasonic dispersion for 60 min. The CNT/IL mixture was transferred to a centrifuge tube and centrifuged at 9,300 × *g* (centrifugal force) for 15 min (Figure S30) to obtained gel. A 0.1 g gel electrolyte was used in all quasi-solid-state Na-CO_2 batteries.

Preparation of the catalyst layer

The catalyst layer for the quasi-solid-state Na-CO_2 battery comprised a gas-diffusion layer (GDL) and a catalyst layer. The catalyst layer was fabricated as per the following steps: (1) conductive carbon (15 mg) and PTFE emulsion (10 mL, 5 wt %) were ultrasonically mixed for 60 min, followed by immersion of a pre-knocked carbon paper (Toray 060, Tokyo, Japan) with a diameter of 1 cm in the solution for 30 min, (2) the treated carbon paper was dried at 60°C and calcined at 450°C for 60 min to obtain the GDL, and (3) the catalyst layer was prepared by dispersing 15 mg of Co-NCF, NCF, commercial Ru/C, or N-CNT in ethanol (2 mL) with a drop of PTFE (0.5 mL, 5 wt %) to obtain catalyst ink. Subsequently, the catalyst ink was homogeneously dropped onto the GDL. The catalyst with a mass of 2 mg cm^{-2} was loaded on the GDL.

Assembling the quasi-solid-state Na-CO_2 battery

In this study, the anolyte was composed of 1 M $NaClO_4$ in the polar aprotic solvent (1:1) of ethylene carbonate (EC), dimethyl carbonate (DMC), and 1 vol % fluoroethylene carbonate (FEC). A NASICON solid electrolyte with an ionic conductivity of 2.7×10^{-3} S cm^{-1} at 25°C (Figure S31) was used to separate the anolyte from the cathode. The cathode, composed of a gel electrolyte, a catalyst layer, and a GDL (carbon paper), was used to construct the proposed quasi-solid-state Na-CO_2 battery: Na | anolyte | NASICON | gel electrolyte | catalyst layer (Figure S32 and Data S1). The battery assembly was operated in an Ar-filled high-integrity glove box.

Electrochemical measurement

The assembled quasi-solid-state Na-CO_2 batteries were connected to a battery test station and placed in a glass container filled with pure flowing CO_2 (1 atm pressure). A battery tester (CT2001A, Wuhan LAND Electronics) was used for electrochemical performance tests at 30°C.

Characterization techniques

XRD (MXP3TA, Mac Science) image of Co-NCF was carried out using an X-ray diffractometer equipped with Cu-Kα radiation in the range of 10°–90° with a scanning rate of 0.02° s^{-1}. Morphologies and microstructures were investigated by SEM (VEGA-3SBH, TESCAN) using an acceleration voltage of 5.0 kV. TEM (JEM-2100, JEOL) images were acquired at an accelerating voltage of 300 kV. The SSAs of the as-prepared materials were calculated using N_2 adsorption-desorption isotherms (BET; Quadrasorb-evo, Quantachrome), and the pore-size distribution was calculated using the BJH method. XPS (PHI5000, PHI) data were collected using a Kα instrument. A differential scanning calorimeter (MELER/1600H, Mettler Toledo) was used for

thermogravimetric analysis (TGA) from room temperature to 700°C in ambient N_2 conditions at a scanning rate of 10°C min^{-1}. The electrochemical workstation (Solartron 1260A, Ametek) was used to measure the EIS of the gel electrolyte under an open-circuit voltage, with an alternating current (AC) interference signal of 20 mV and a frequency range of 0.01–50 kHz. Raman spectra (Renishaw in Via, Renishaw) were recorded under laser excitation at 514 nm (2.41 eV) over a spectral range of 3,000–800 cm^{-1} at room temperature. AFM (Dimension Icon, Bruker) images were recorded in the SCAN Assist mode. The LSV measurements are composed of sodium (counter electrode), NASICON, and gel (with or without NaTFSI) as the work electrode. It was performed from 1 to 5 V with a scan rate of 0.1 mV s^{-1}. The ionic conductivity of the gel was measured by EIS using an impedance/gain-phase analyzer (Solartron 1260A, Ametek) with test molds composed of the gel and two blocking electrodes (stainless steel).[51] The ionic conductivity, σ (S cm^{-1}), was calculated using the following equation:

$$\sigma = L/(R \times A)$$

where L (cm) and A (cm^2) are the thickness and cross-sectional area of the gel, respectively, and R (Ω) is the total electrolyte resistance.

Computational details

All DFT computations were performed using the DMol3 software package, based on the linear combination of atomic orbitals (LCAO) method.[52,53] Electron-ion interactions were described using all-electron potentials. A double numerical polarized (DNP) basis set was used to expand the wave functions, with orbital cutoffs of 3.7, 3.3, 4.5, and 3.4 Å for C, O, Co, and N, respectively. The Perdew-Burke-Ernzerhof (PBE) functional was used for the electron-electron exchange and correlation interactions, while van der Waals interactions were described using the dispersion correction (DFT-D2) method proposed by Grimme.[54] In this study, the convergence criterion for the electronic self-consistent field (SCF) loop was set to 10^{-6}.[55] The atomic structures were optimized until the residual forces were <0.004 Ha $Å^{-1}$. The Gibbs free energy of the reaction step is calculated by equation via the finite difference method with the step size of 0.015 Å:

$$\Delta G = \Delta E + \Delta ZPE - T\Delta S$$

where ΔE (eV) is the electronic energy difference based on DFT calculations, ΔZPE (eV) is the change in zero-point energy, T is the temperature (equal to 298.15 K here), and ΔS (kJ mol^{-1} K^{-1}) is the change in the entropy. The zero-point energy and entropy were obtained through vibrational frequencies.

SUPPLEMENTAL INFORMATION

Supplemental information can be found online at https://doi.org/10.1016/j.xcrp.2022.100973.

ACKNOWLEDGMENTS

This work is financially supported by the National Natural Science Foundation of China (12175089); the National Key Research and Development Program of China (no. 2019YFC1907900); the Joint Construction of China-Japan Plasma Laboratory (no. KKPA202152002); the Key Research and Development Program of Yunnan Province (202103AF140006 and 202103AM140003); the Applied Basic Research Programs of Yunnan Provincial Science and Technology Department (202001AW070004); and the Key Laboratory of Resource Chemistry, Ministry of Education (KLRC V_ME2001).

AUTHOR CONTRIBUTIONS

B.X., D.Z., and F.L. conceived and designed the study. B.X., D.Z., and S.C. designed the experiments and collected and analyzed the data. C.P. carried out the theoretical/DFT calculations. M.H., Y.L., D.X., and B.Y. assisted with the experiments and characterizations. B.X. wrote the manuscript. B.X., D.Z., and F.L. discussed the results and prepared the manuscript. All authors reviewed and contributed to this paper.

DECLARATION OF INTERESTS

The authors declare no competing interests.

Received: March 31, 2022
Revised: May 18, 2022
Accepted: June 14, 2022
Published: July 12, 2022

REFERENCES

1. Xie, J., and Wang, Y. (2019). Recent development of CO_2 electrochemistry from Li–CO_2 batteries to Zn–CO_2 batteries. Acc. Chem. Res. *52*, 1721–1729.

2. Wang, F., Li, Y., Xia, X., Cai, W., Chen, Q., and Chen, M. (2021). Metal–CO_2 electrochemistry: from CO_2 recycling to energy storage. Adv. Energy Mater. *11*, 2100667.

3. Nguyen, D.L.T., Kim, Y., Hwang, Y.J., and Won, D.H. (2020). Progress in Development of Electrocatalyst for CO_2 conversion to selective CO production. Carbon Energy *2*, 72–98.

4. Hu, X., Sun, J., Li, Z., Zhao, Q., Chen, C., and Chen, J. (2016). Rechargeable room–temperature Na–CO_2 batteries. Angew. Chem. Int. Ed. *55*, 6482–6486.

5. Larcher, D., and Tarascon, J.M. (2015). Towards greener and more sustainable batteries for electrical energy storage. Nat. Chem. *7*, 19–29.

6. Chen, B., Zhong, X., Zhou, G., Zhao, N., and Cheng, H. (2022). Graphene–supported atomically dispersed metals as bifunctional catalysts for next–generation batteries based on conversion reactions. Adv. Mater. *34*, 2105812.

7. Xing, Y., Yang, Y., Li, D., Luo, M., Chen, N., Ye, Y., Qian, J., Li, L., Yang, D., and Wu, F.J. (2018). Crumpled Ir nanosheets fully covered on porous carbon nanofibers for long–life rechargeable lithium–CO_2 batteries. Adv. Mater. *30*, 1803124.

8. Li, J., Dai, A., Amine, K., and Lu, J. (2021). Correlating catalyst design and discharged product to reduce overpotential in Li–CO_2 batteries. Small *17*, 2007760.

9. Feng, N., Wang, B., Yu, Z., Gu, Y., Xu, L., Ma, J., Wang, Y., and Xia, Y. (2021). Mechanism–of–Action elucidation of reversible Li–CO_2 batteries using the water–in–salt electrolyte. ACS Appl. Mater. Interfaces *13*, 7396–7404.

10. Zhang, Z., Bai, W.L., Cai, Z.P., Cheng, J.H., Kuang, H.Y., Dong, B.X., Wang, Y.B., Wang, K.X., and Chen, J.S. (2021). Enhanced electrochemical performance of aprotic Li–CO_2 batteries with a ruthenium–complex–based mobile catalyst. Angew. Chem. Int. Ed. Engl. *60*, 16404–16408.

11. Yu, X., and Manthiram, A. (2020). Recent advances in lithium–carbon dioxide batteries. Small Structures *1*, 2000027.

12. Zhang, K., Zhang, Y., Zhang, Q., Liang, Z., Gu, L., Guo, W., Zhu, B., Guo, S., and Zou, R. (2020). Metal–Organic Framework–Derived Fe/Cu–substituted Co nanoparticles embedded in CNTs–grafted carbon polyhedron for Zn–air batteries. Carbon Energy *2*, 283–293.

13. Li, G., Lei, W., Luo, D., Deng, Y., Deng, Z., Wang, D., Yu, A., and Chen, Z. (2018). Stringed "tube on Cube" nanohybrids as compact cathode matrix for high–loading and lean–electrolyte lithium–sulfur batteries. Energy Environ. Sci. *11*, 2372–2381.

14. Jian, S., Hsiao, L., Yeh, M., and Ho, K. (2019). Designing a carbon nanotubes-interconnected ZIF-derived cobalt sulfide hybrid nanocage for supercapacitors. J. Mater. Chem. *7*, 1479–1490.

15. Zhang, J., Meng, Z., Yang, D., Song, K., Mi, L., Zhai, Y., Guan, X., and Chen, W. (2022). Enhanced interfacial compatibility of FeS@N, S–C anode with ester–based electrolyte enables stable sodium–ion full cells. J. Energy Chem. *68*, 27–34.

16. Wang, X.R., Liu, J.Y., Liu, Z.W., Wang, W.C., Luo, J., Han, X.P., Du, X.W., Qiao, S.Z., and Yang, J. (2018). Identifying the Key role of pyridinic–N–Co bonding in synergistic electrocatalysis for reversible ORR/OER. Adv. Mater. *30*, 1800005.

17. Wu, Z.Z., Gao, F.Y., and Gao, M.R. (2021). Regulating the oxidation state of nanomaterials for electrocatalytic CO_2 reduction. Energy Environ. Sci. *14*, 1121–1139.

18. You, S., Gong, X., Wang, W., Qi, D., Wang, X., Chen, X., and Ren, N. (2016). Enhanced cathodic oxygen reduction and power production of microbial fuel cell based on noble–metal–free electrocatalyst derived from metal–organic frameworks. Adv. Energy Mater. *6*, 1501497.

19. Yang, X., Su, F., Hou, M., Zhang, D., Dai, Y., and Liang, F. (2021). Plasma tailored reactive nitrogen species in MOF derived carbon materials for hybrid sodium–air batteries. Dalton Trans. *50*, 7041–7047.

20. Song, K., Liu, J., Dai, H., Zhao, Y., Sun, S., Zhang, J., Qin, C., Yan, P., Guo, F., and Wang, C. (2021). Atomically dispersed Ni induced by ultrahigh N–doped carbon enables stable sodium storage. Chem *7*, 2684–2694.

21. Xu, C., Wang, H., Zhan, J., Kang, Y., and Liang, F. (2022). Engineering NH_3–induced 1D self–assembly architecture with conductive polymer for advanced hybrid Na–CO_2 batteries via morphology modulation. J. Power Sources *520*, 230909.

22. Lu, Q., Zou, X., Liao, K., Ran, R., Zhou, W., Ni, M., and Shao, Z. (2020). Direct growth of ordered N–doped carbon nanotube Arrays on carbon fiber cloth as A free–standing and binder–free air electrode for flexible quasi–solid–state rechargeable Zn–air batteries. Carbon Energy *2*, 461–471.

23. Li, W., Liu, B., Liu, D., Guo, P., Liu, J., Wang, R., Guo, Y., Tu, X., Pan, H., and Sun, D. (2022). Alloying Co species into ordered and interconnected macroporous carbon polyhedra for efficient oxygen reduction reaction in rechargeable zinc–air battery. Adv. Energy Mater. *34*, 2109605.

24. Mohd Adli, N., Shan, W., Hwang, S., Samarakoon, W., Karakalos, S., Li, Y., Cullen, D.A., Su, D., Feng, Z., and Wang, G. (2021). Engineering atomically dispersed FeN_4 active sites for CO_2 electroreduction. Angew. Chem. Int. Ed. Engl. *133*, 1035–1045.

25. Wu, M., Zhang, G., Hu, Y., Wang, J., Sun, T., Regier, T., Qiao, J., and Sun, S. (2021). Graphitic–shell encapsulated FeNi alloy/nitride nanocrystals on biomass–derived N–doped carbon as an efficient electrocatalyst for rechargeable Zn–air battery. Carbon Energy *3*, 176–187.

26. Almdal, K., Dyre, J., Hvidt, S., and Kramer, O. (1993). Towards A phenomenological

definition of the term 'gel'. Polym. Gels Netw. *1*, 5–17.

27. Ruoff, R.S., Tersoff, J., Lorents, D.C., Subramoney, S., and Chan, B. (1993). Radial deformation of carbon nanotubes by van der Waals forces. Nature *364*, 514–516.

28. Ma, J.C., and Dougherty, D.A. (1997). The cation–π interaction. Chem. Rev. *97*, 1303–1324.

29. Fukushima, T., Kosaka, A., Ishimura, Y., Yamamoto, T., Takigawa, T., Ishii, N., and Aida, T. (2003). Molecular ordering of organic molten salts triggered by single–walled carbon nanotubes. Science *300*, 2072–2074.

30. Zhang, T., and Zhou, H. (2012). From *Li–O_2* to Li–air batteries: carbon nanotubes/ionic liquid gels with a tricontinuous passage of electrons, ions, and oxygen. Angew. Chem. Int. Ed. Engl. *51*, 11062–11067.

31. Chang, S., Hou, M., Xu, B., Liang, F., Qiu, X., Yao, Y., Qu, T., Ma, W., Yang, B., and Dai, Y. (2021). High–performance quasi–solid–state Na–air battery via gel cathode by confining moisture. Adv. Funct. Mater. *31*, 2011151.

32. Maciel, I.O., Anderson, N., Pimenta, M.A., Hartschuh, A., Qian, H., Terrones, M., Terrones, H., Campos Delgado, J., Rao, A., and Novotny, L. (2008). Electron and phonon renormalization at defect/doping sites in carbon nanotubes. Nat. Mater. *7*, 878–883.

33. Jiao, L., Zhang, L., Wang, X., Diankov, G., and Dai, H. (2009). Narrow graphene nanoribbons from carbon nanotubes. Nature *458*, 877–880.

34. Basile, A., Hilder, M., Makhlooghiazad, F., Pozo–Gonzalo, C., MacFarlane, D.R., Howlett, P.C., and Forsyth, M. (2018). Ionic liquids and organic ionic plastic crystals: advanced electrolytes for safer high performance sodium energy storage technologies. Adv. Energy Mater. *8*, 1703491.

35. Mu, X., Pan, H., He, P., and Zhou, H. (2020). *Li–CO_2 and Na–CO_2* batteries: toward greener and sustainable electrical energy storage. Adv. Mater. *32*, 1903790.

36. Liang, F., Zhang, K., Zhang, L., Zhang, Y., Lei, Y., and Sun, X. (2021). Recent development of electrocatalytic CO_2 reduction application to energy conversion. Small *17*, 2100323.

37. Xu, C., Zhan, J., Wang, Z., Fang, X., Chen, J., Liang, F., Zhao, H., and Lei, Y. (2021). Biomass–derived highly dispersed Co/Co_9S_8 nanoparticles encapsulated in S, N–co–doped hierarchically porous carbon as an efficient catalyst for hybrid Na–CO_2 batteries. Mater. Today Energy *19*, 100594.

38. Hou, Y., Wang, J., Liu, L., Liu, Y., Chou, S., Shi, D., Liu, H., Wu, Y., Zhang, W., and Chen, J. (2017). Mo_2C/CNT: an efficient catalyst for rechargeable LiCO_2 batteries. Adv. Funct. Mater. *27*, 1700564.

39. Shippey, T.A. (1980). Vibrational studies of anhydrous lithium, sodium and potassium oxalates. J. Mol. Struct. *67*, 223–233.

40. Zhu, Q., Xu, S., Cai, Z., Harris, M., Wang, K., and Chen, J. (2017). Towards real Li–air batteries: a binder–free cathode with high electrochemical performance in CO_2 and O_2. Energy Storage Mater. *7*, 209–215.

41. Fang, C., Luo, J., Jin, C., Yuan, H., Sheng, O., Huang, H., Gan, Y., Xia, Y., Liang, C., and Zhang, J. (2018). Enhancing catalyzed decomposition of Na_2CO_3 with Co_2MnOx nanowire–decorated carbon fibers for advanced Na–CO_2 batteries. ACS Appl. Mater. Interfaces *10*, 17240–17248.

42. Hu, X., Li, Z., Zhao, Y., Sun, J., Zhao, Q., Wang, J., Tao, Z., and Chen, J. (2017). Quasi–solid state rechargeable Na–CO_2 batteries with reduced graphene oxide Na anodes. Sci. Adv. *3*, e1602396.

43. Lu, Y., Das, S.K., Moganty, S.S., and Archer, L.A. (2012). Ionic liquid–nanoparticle hybrid electrolytes and their application in secondary lithium–metal batteries. Adv. Mater. *24*, 4430–4435.

44. Li, C., Gu, L., Tong, J., and Maier, J. (2011). Carbon nanotube wiring of electrodes for high–rate lithium batteries using an imidazolium–based ionic liquid precursor as dispersant and binder: a case study on iron fluoride nanoparticles. ACS Nano *5*, 2930–2938.

45. Yang, J., Chen, H.Q., Shi, N., Wang, T., Liu, J., and Pan, W.P. (2022). Porous carbon with uniformly distributed cobalt nanoparticles derived from ZIF–67 for efficient removal of vapor elemental mercury: a combined experimental and DFT study. Chem. Eng. J. *428*, 132095.

46. Kang, Y., Wang, S., Zhu, S., Gao, H., San Hui, K., Yuan, C., Yin, H., Bin, F., Wu, X., and Mai, W. (2021). Iron-modulated nickel cobalt phosphide embedded in carbon to boost power density of hybrid sodium–air battery. Appl. Catal. B *285*, 119786.

47. Zhou, J., Li, X., Yang, C., Li, Y., Guo, K., Cheng, J., Yuan, D., Song, C., Lu, J., and Wang, B.J. (2019). A quasi–solid–state flexible fiber–shaped Li–CO_2 battery with low overpotential and high energy efficiency. Adv. Mater. *31*, 1804439.

48. Wu, Y., Qiu, X., Liang, F., Zhang, Q., Koo, A., Dai, Y., Lei, Y., and Sun, X. (2019). A metal–organic framework–derived bifunctional catalyst for hybrid sodium–air batteries. Appl. Catal. B *241*, 407–414.

49. Wang, X., Zhou, J., Fu, H., Li, W., Fan, X., Xin, G., Zheng, J., and Li, X. (2014). MOF derived catalysts for electrochemical oxygen reduction. J. Mater. Chem. *2*, 14064–14070.

50. Xia, B., Yan, Y., Li, N., Wu, H., Lou, X., and Wang, X. (2016). A metal–organic framework–derived bifunctional oxygen electrocatalyst. Nat. Energy *1*, 1–8.

51. Wang, S., Yan, M., Li, Y., Vinado, C., and Yang, J.J. (2018). Separating electronic and ionic conductivity in mix–conducting layered lithium transition–metal oxides. J. Power Sources *393*, 75–82.

52. Zhu, J., Wu, W., and Fisher, A.J. (2020). Linear combination of atomic orbitals model for deterministically placed acceptor arrays in silicon. Phys. Rev. B *101*, 085303.

53. Dahéron, L., Martinez, H., Dedryvere, R., Baraille, I., Ménétrier, M., Denage, C., Delmas, C., and Gonbeau, D. (2009). Surface properties of $LiCoO_2$ investigated by XPS analyses and theoretical calculations. J. Phys. Chem. C *113*, 5843–5852.

54. Bucko, T., Hafner, J., Lebegue, S., and Angyán, J.G. (2010). Improved description of the structure of molecular and layered crystals: Ab initio DFT calculations with van der Waals corrections. J. Phys. Chem. A *114*, 11814–11824.

55. Zhou, Y., Saad, Y., Tiago, M.L., and Chelikowsky, J.R.J. (2006). Self–consistent–field calculations using Chebyshev–filtered subspace iteration. J. Comput. Phys. *219*, 172–184.